Graphical Abstract

Boron-Doped Polysilicon Using Spin-On Doping for High-Efficiency Both-Side Passivating Contact Silicon Solar Cells

HyunJung Park, Jinsol Kim, Dongjin Choi, Sang-Won Lee, Dongkyun Kang, Hae-Seok Lee, Donghwan Kim, Munho Kim, Yoonmook Kang

The passivation quality of the p^+ poly-Si passivating contacts with boron SOD was investigated. The factors influencing the passivation quality of p^+ poly-Si are crystallinity, indiffusion, and doping concentration. A 17.5% efficiency with 695 mV V_{OC} was achieved by controlling the process parameters with optimization and simulation, reaching the highest reported cell efficiency with SOD p^+ poly-Si on saw-damage-removed flat surfaces.

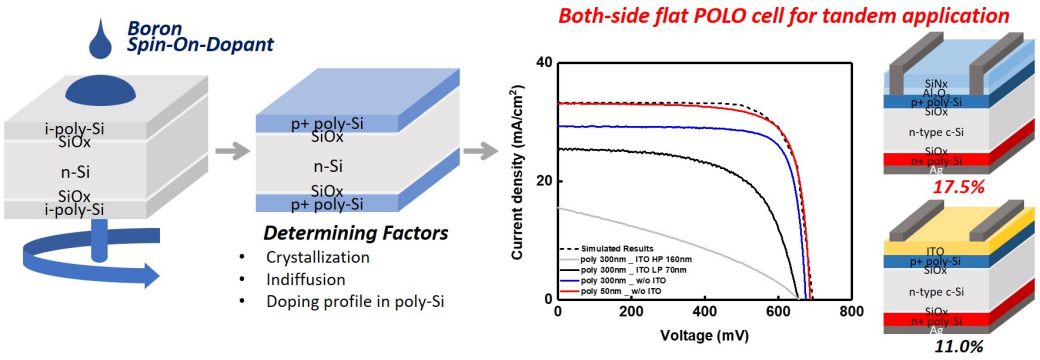

Highlights

Boron-Doped Polysilicon Using Spin-On Doping for High-Efficiency Both-Side Passivating Contact Silicon Solar Cells

HyunJung Park, Jinsol Kim, Dongjin Choi, Sang-Won Lee, Dongkyun Kang, Hae-Seok Lee, Donghwan Kim, Munho Kim, Yoonmook Kang

- The passivation quality of p^+ poly-Si passivating contacts with boron SOD was investigated.
- The factors influencing the passivation quality of p^+ poly-Si were crystallinity (grain size), indiffusion of boron into the bulk, and doping concentration (field effect).
- The doping process was further optimized by controlling the boron indiffusion from the SOD source to c-Si bulk using an additional diffusion barrier layer that controls the boron doping profile.
- Poly-Si contact cells with both-side flat surfaces and poly-Si contacts showed a maximum efficiency of 17.5% with V_{OC} of 695 mV when a developed p^+ poly-Si was applied at the front. This is the highest reported efficiency using boron-SOD-doped p^+ poly-Si emitter on saw-damage-removed flat surfaces.
- Based on a wide range of analyses and experimental results, a 3D energy band diagram of p^+ poly-Si/SiO_x/c-Si passivating contacts is exhibited.
- The cell result validates its potential for use in silicon-based tandem solar cells and the efficiency can be further improved by applying textured surfaces, FGA, and selective emitter for improved metal contacts.

Boron-Doped Polysilicon Using Spin-On Doping for High-Efficiency Both-Side Passivating Contact Silicon Solar Cells

HyunJung Park[a,b,1], Jinsol Kim[c,1], Dongjin Choi[c], Sang-Won Lee[a], Dongkyun Kang[c], Hae-Seok Lee[d], Donghwan Kim[c], Munho Kim[b,*], Yoonmook Kang[d,*]

[a]*Institute for Energy Research, Korea University, 145, Anam-ro, Seongbuk-gu, 02841, Seoul, Republic of Korea*
[b]*School of Electrical and Electronic Engineering, Nanyang Technological University, 50 Nanyang Avenue, 639798, Singapore, Singapore*
[c]*Department of Materials Science and Engineering, Korea University, 145, Anam-ro, Seongbuk-gu, 02841, Seoul, Republic of Korea*
[d]*KU-KIST Green School Graduate School of Energy and Environment, Korea University, 145, Anam-ro, Seongbuk-gu, 02841, Seoul, Republic of Korea*

Abstract

This study focuses on boron-doped p^+polysilicon (poly-Si) passivating contacts using spin-on doping (SOD). Experimental conditions, including annealing conditions, SOD concentration, and poly-Si thickness, were controlled to improve passivation. Based on the analysis results, the passivation quality mainly changes with indiffusion and doping concentration, causing Auger recombination and field effects. Meanwhile, grain size also influences the passivation quality but showed marginal characteristics. Through further optimization using an etch-back and diffusion barrier, the efficiency of the flat reference solar cell was improved to 17.5% with an open-circuit voltage of 695 mV using a p^+ poly-Si contact emitter, the highest reported efficiency using SOD on saw-dagame-etched surfaces. This study includes a detailed analysis of SOD p^+ poly-Si and shows promising results with potential for application in tandem devices. Furthermore, the cell efficiency is expected to

*Corresponding author
Email addresses: munho.kim@ntu.edu.sg (Munho Kim), ddang@korea.ac.kr (Yoonmook Kang)
[1]These authors contributed equally

increase by controlling the doping profile and application of textured surfaces, selective emitters, and forming gas annealing (FGA).

Keywords: Crystalline silicon, solar cells, passivating contact, boron-doped polysilicon, passivated emitter, spin-on doping, tunnel oxide

1. Introduction

Aluminum and silicon in conventional silicon solar cells, such as back-surface field and passivated emitter and rear cell, have direct contact. This is the principal cause of low efficiency compared with other high-efficiency cells. High-efficiency silicon solar cells are based on high-quality passivation schemes that use the insertion of a thin passivation layer between the metal and silicon. This passivation layer effectively suppresses recombination, which improves cell performance. Amorphous silicon (a-Si:H) or silicon oxide (SiO_x) is generally used as the passivation layer. Cells that use a-Si:H as a passivation layer are called heterojunction cells. The record efficiency of heterojunction cells is 26.7% [1] with an interdigitated back contact (IBC) structure. However, a-Si:H is vulnerable to high-temperature processes, which restricts its usage and subsequent process temperature [2]. Therefore, another type of high-efficiency passivating contact cell, consisting of poly-Si and nanoscale thin tunnel oxide based on high-temperature annealing processes for crystallization of the poly-Si layer, named polysilicon (poly-Si) passivating contacts is employed. In this poly-Si passivating contact, the tunnel oxide prevents direct contact between the metal and bulk silicon, thereby reducing recombination losses. In addition, the tunnel oxide functions as a passivation layer that allows majority carriers to flow by tunneling and avoids the flow of minority carriers into the defective poly-Si layer, leading to high carrier selectivity and an increase in cell efficiency [3, 4, 5, 6, 7]. The cells fabricated with rear n^+ poly-Si contact and front BBr_3-diffused emitter showed a record efficiency of 26.0% [8]. The cell with p^+ and n^+ poly-Si passivating contacts for hole and electron contacts, respectively, can further reduce recombination originating from both types of contacts and improve cell efficiency. The reported world record of all poly-Si passivating contact cells is 26.1% [9] using the IBC structure. Many studies on n^+ poly-Si passivating contacts have been conducted, and the applications of n^+ poly-Si contacts have shown promising cell results owing to an increase in the passivation quality [1, 2, 3]. The fabrication and role of n^+

poly-Si have also been studied extensively [10, 11]. The formation of n^+ poly-Si can be divided into two groups depending on the doping method: in-situ, which is an application of phosphorus-doped n^+ poly-Si, and ex-situ doping, which involves the doping of phosphorus on intrinsic poly-Si [11, 12]. As the control of phosphorus is easier than that of boron, and the activation of the atom can be obtained at a lower temperature [13], both in-situ and ex-situ-doped n^+ poly-Si show high passivation qualities. For in-situ doping, the carriers can be easily trapped inside the poly-Si, and only a few atoms are allowed to tunnel through the tunnel oxide. Additional annealing is still required to crystalize the poly-Si layer and activate the dopants. With optimized annealing time and temperature, implied open-circuit voltages (iV_{OC}) as high as 740 mV and a lifetime of 1210 µs have been obtained [12]. Several ex-situ-based phosphorus doping methods exist; however, the most commonly used method is $POCl_3$ diffusion using a tube furnace. Because the phosphorus concentration in the source layer deposited by $POCl_3$ diffusion ($>4 \times 10^{21}$ cm^{-3}) is higher than that of in-situ doping ($<2 \times 10^{20}$ cm^{-3}), the passivation quality is slightly lower than that of the in-situ layer, resulting in a high iV_{OC} over 730 mV [14, 15, 11]. These results demonstrate the excellent passivation quality of passivating contacts using tunnel oxide and doped poly-Si structures. Owing to the more sensitive diffusion conditions of boron, fewer studies on p^+ poly-Si layers have been conducted [16, 17, 18, 19, 20, 21, 22, 23, 24, 25, 26, 27, 28] compared with n^+ poly-Si. This also results from the difficulty in doping silicon with boron because of the lower effective diffusivity and surface doping concentration of B in Si compared to that of P under the same annealing conditions [29, 30]. Additionally, the role of p^+ poly-Si and the tunnel oxide structure, which can be used as an emitter, has not been studied. Therefore, this study investigates p^+ poly-Si passivating contacts, focusing on the role of p^+ poly-Si using a simple doping process. Using a spin-on doping (SOD) source, a source layer can be easily formed on one side, and the characteristics can be simply controlled by changing the SOD concentration, annealing time, and temperature. SOD is a process in which a dopant source is applied and spread evenly by spin coating. Subsequently, a pre-bake was performed to evaporate the solvent, followed by high-temperature annealing in an N_2 atmosphere to diffuse the dopant atoms. The borosilicate glass (BSG) layer formed during high-temperature annealing was removed by HF dipping [17]. Different sources exist; however, the solvent is generally ethanol. This SOD process is suitable for single-side doping; meanwhile, the BBr_3 diffusion process forms double-

side doping, requiring additional process steps to enable single-side doping, such as the deposition of a diffusion barrier or single-side etching. In addition, the junction depth can be easily controlled when using SOD. This can be achieved by simply changing the SOD source or annealing temperature and time [16, 17]. However, the SOD method is limited by the formation of a boron-rich layer (BRL) at the surface owing to the high concentration of boron in the SOD source [31]. This causes the formation of recombination centers at the surface and decreases passivation quality. Therefore, this study investigates the role of p^+ poly-Si formed using a conventional SOD boron source as a passivating emitter. Moreover, a wide range of analysis results was demonstrated to validate the impact of crystallinity and indiffusion on passivation quality, including the grain size of poly-Si, doping concentration profile, Auger simulations, and surface recombination. As a result, this study developed a 3D energy band diagram of p^+ poly-Si passivating contacts. The fabrication process for p^+ poly-Si with SOD was further optimized by controlling the variables and applying etch-back and diffusion barriers, leading to an increased open-circuit voltage (V_{OC}) and higher cell efficiency.

2. Experiments

This study used the Czochralski method with n-type crystalline silicon (c-Si) wafers. The wafer thickness and resistivity were 180 µm and 1 Ω·cm, respectively. Subsequently, saw-damage etching and RCA cleaning were performed, followed by chemical growth of a silicon oxide layer (<2 nm) using H_2O_2 [32]. Next, the intrinsic poly-Si layer was deposited on top of the silicon oxide layer using a low-pressure chemical vapor deposition (LPCVD) system at 600 °C. Poly-Si thicknesses of 300 and 50 nm were used to study the effect of thickness on passivation. Double-side-deposited samples were used for the preliminary tests (pre-tests) (Fig. 1 (a)); however, single-side etching was performed using TMAH at 80 °C for 30 s when cell-like samples were fabricated (Fig. 1 (b) and (c)). An SOD source with concentration variations of 4% (B155 spin-on dopant, Filmtronics) and 2% (B153 spin-on dopant, Filmtronics) was applied after poly-Si deposition. A spin coater was used at 5000 rpm for uniform coating. The samples were annealed in a tube furnace under an N_2 atmosphere after pre-baking at 200 °C for 10 min on a hot plate to evaporate the solvent of the source. For the first set of experiments, the dwell time was fixed at 10 min, and the controlled variables were annealing temperature, source concentration, and poly-Si thickness. Follow-

ing high-temperature annealing, the unnecessary SOD and BSG layers were etched by HF dipping. Next, hydrogenation with a stack of SiN_x/Al_2O_3 and subsequent annealing by a rapid thermal process was applied to all the samples to improve the passivation quality. All the analyses were performed after hydrogenation. The passivation quality was evaluated from iV_{OC} and lifetime values measured by quasi-steady-state photoconductance, and the other factors that influence the passivation quality of p^+ poly-Si were confirmed by doping the 300 nm intrinsic poly-Si. In addition to iV_{OC}, the grain size and doping profile were measured for precise analysis using X-ray diffraction (XRD) and secondary ion mass spectrometry (SIMS). The same experiment was repeated using a thin poly-Si layer (50 nm). The poly-Si thickness was reduced to use the p^+ poly-Si passivating contact at the front side as an emitter as the parasitic absorption loss increases for thicker p^+ poly-Si layers. The same measurements, including iV_{OC}, grain size, and doping profile, were conducted again for 50 nm p^+ poly-Si. Based on the analysis results, the doping of thin poly-Si with SOD was further optimized. Using the measured doping profiles, the diffusion length and recombination characteristics were calculated using the EDNA2 program [33], and the annealing temperature and time were optimized by summing up the pre-tests. Finally, both sides of the poly-Si passivating contact cells (Fig. 1 (b) and (c)) were fabricated with optimized p^+ poly-Si layers following the cell fabrication procedure in Fig. 1 (d). In-situ n^+ poly-Si was deposited on both sides, and single-side n^+ poly-Si was etched off using the TMAH solution, followed by the same deposition procedure and etching for intrinsic poly-Si. Next, the SOD source was coated on the intrinsic poly-Si layer with the application of a SiO_x doping barrier on the other side to protect n^+ poly-Si from dopant compensation. Subsequently, the samples were annealed to crystallize both-side poly-Si layers, followed by hydrogenation. A front-side metal contact electrode was then formed by photolithography and evaporation of a Ti (50 nm)/Pd (50 nm)/Ag (1 µm) stack, followed by rear-side electrode formation by the full-area deposition of Ag (1 µm) without a pattern. Finally, cell characteristics were analyzed using light current-voltage (LIV) measurements. The size of the fabricated cells was $2\,\text{cm} \times 2\,\text{cm}$.

3. Results and discussion

3.1. Analysis of the SOD source

Conventionally, the boron concentration in the BSG layer used as an emitter can be calculated as 5×10^{21} cm^{-3} [34]. Before calculating the boron concentration in the SOD source, the elements included in the source were analyzed using Auger electron spectroscopy (AES) [35]. The results are shown in Fig. 2; from these results, the main elements included in the source could be analyzed, which were B, C, and O, as shown in Fig. 2 (a) and A.10. Based on the scanning electron microscopy (SEM) image, the thickness of the spin-coated SOD source layer was 86.96 nm (Fig. 2 (b)). The atomic concentration of the source was calculated based on a density of 1.097 g/cm^3 measured by an electronic analytical balance. Therefore, the chosen SOD sources with dopant compound concentrations of 4% and 2% had boron concentrations of 6.5×10^{21} cm^{-3} and 2.4×10^{21} cm^{-3}, respectively. The SOD source with a higher and one with a lower boron concentration than that of the conventional BSG layer formed by BBr_3 diffusion were chosen. Throughout the experiments, concentrations of 4% and 2% were used and compared in terms of their diffusion profiles and passivation qualities in p^+ poly-Si contacts.

3.2. Preliminary tests on p^+ poly-Si

3.2.1. 300 nm poly-Si

An intrinsic poly-Si of 300 nm thick was deposited and doped using SOD on both sides to investigate the factors contributing to the passivation quality. The annealing conditions were varied to control the passivation quality. The source concentration and annealing temperature were varied, whereas the dwell time was fixed at 10 min. The results are shown in Fig. 3 (a). (Here, Fig. 3 (b) shows the results with a thinner p^+ poly-Si of 50 nm, which is discussed in the following subsection.) Using p^+ poly-Si of 300 nm thick, with SOD sources 4% and 2%concentration, the passivation quality increased up to 950 °C and started decreasing for annealing temperatures beyond 950 °C. A detailed analysis was conducted in two directions, one analyzing the crystallization and the other analyzing the doping concentration profile.

(i) Crystallization of poly-Si

First, the crystallization of poly-Si after high-temperature annealing was analyzed using transmission electron microscopy (TEM). TEM images of poly-Si before and after annealing at 950 °C (highest iV_{OC}) were compared.

In Fig. 4 (a), the TEM image showed that the thickness of as-deposited intrinsic poly-Si was 308 nm before annealing. After annealing, crystallization of the poly-Si was validated from the diffraction patterns, and the thickness was reduced to 243 nm owing to crystallization, and indiffusion of the boron source [36] (Fig. 4 (b)). However, a precise comparison of crystallization could not be performed using TEM images alone. XRD patterns were measured to calculate the grain size of poly-Si according to the annealing time and temperature to compare the crystallinity with precision. The measured XRD patterns are shown in Fig. 5 (a). The grain size was calculated using Scherrer equation [37]. Annealing temperatures of 900, 950, and 1000 °C were maintained for a fixed dwell time of 10 min. In addition, dwell times of 20 and 30 min were investigated at 950 °C. A change in the passivation quality according to the grain size was observed when the annealing time was increased from 20 to 30 min (Fig. 5 (b)). The sheet resistances after annealing for 10, 20, and 30 min were 117.2, 92.45, and 89.68 Ω/sq, respectively. Thus, it can be predicted that more indiffusion into the bulk silicon occurs (assuming the concentration in poly-Si is equal owing to the same annealing temperature). However, the iV_{OC} increased from 635.6 mV in 20 min to 649.3 mV in 30 min, owing to a significant increase in the grain size from 19.44 nm to 51.54 nm (Fig. 5 (a) and (b)). We can infer that the passivation quality of the poly-Si layer was improved because of the increase in grain size when considering the data except for the sample annealed at 900 °C for 10 min. The effect of grain size on the passivation quality is as follows. Unlike the band alignment at the grain, holes were depleted at the defective grain boundaries, changing the alignment of the bandgap energy (Fig. 5 (e)). Because of the lower energy barrier at the grain boundary, minority carriers, which are electrons, in this case when considering p^+ poly-Si, can then diffuse into p^+ poly-Si and recombine with the trapped holes, decreasing the passivation quality. Therefore, the increased average grain size can result in higher iV_{OC} values, as shown in Fig. 5 (b). However, SOD p^+ poly-Si also had a buried PN junction, which is a heavily doped indiffused region underneath SiO_x, as observed from the SIMS profile (Fig. 6 (a)). This buried junction lowers the energy barrier, carrier selectivity, and passivation quality, and consequently reduces the impact of crystallinity. This trend of passivation quality according to the grain size and indiffusion obtained in this study is similar to the trend of n^+ poly-Si contacts shown in our previous study [11].

(ii) Boron doping profile

The boron doping concentration profile was measured for a 4% source 900 °C, 950 °C, and 1000 °C annealed samples to analyze the indiffusion and field-effect passivation. In Fig. 6 (a), the doping profile of 300 nm p^+ poly-Si shows a constant concentration in the poly-Si and a drop in the concentration after the tunnel oxide. (The position of the tunnel oxide was determined at the peak position of the oxygen intensity, as shown in Fig. 6 (a) and (c)) In addition, the doping concentration in the poly-Si changed with the annealing temperature. The doping concentration of poly-Si was saturated at the solubility limit of the annealing temperature, except for 900 °C, where the measured concentration was considerably below the solubility limit [38, 39]. In summary, the passivation quality was improved because of the difference in the doping concentration of poly-Si and bulk c-Si. The thin tunnel oxide between the poly-Si layer and bulk c-Si acted as a barrier to reduce boron diffusion from poly-Si to bulk c-Si, leading to a sudden difference in the doping concentration, which improves the passivation quality via the field effect [40, 41, 42]. This result is indicated by the increase in iV_{OC} from 900 °C to 950 °C. Furthermore, the passivation quality was influenced by indiffusion into bulk silicon. From the doping profile in Fig. 6 (a) and (c), as the annealing temperature increased, the number of boron atoms indiffused through the tunnel oxide increased. Based on the doping profiles in Fig. 6 (a) and (c), the Auger recombination limit was calculated using the EDNA2 program [33] (Fig. 6 (b) and (d)). This indicates that a doping profile with more indiffusion increased Auger recombination. The increase in Auger recombination can indicate an increase in inactive clusters of boron because the difference between the solubility limit and the measured doping concentration increased as Auger recombination increased (Fig. 6 (a) and (b)). These inactive boron clusters acted as recombination centers, consequently reducing passivation quality [42, 43]. The drop in iV_{OC} from 661.5 to 639.6 mV at 950 °C and 1000 °C can be explained by this increased indiffusion. In addition, the difference between the $J_{0,Auger}$ limit and measured J_0 increased with increasing temperature, indicating that the other recombination losses also increased, increasing the measured J_0 value. Furthermore, the effective surface recombination velocity (SRV) was extracted from EDNA 2, as shown in Figs. 6 (b) and (d). The extracted SRV values depended on the surface doping concentration, exhibiting a trend similar to that of Wyss et al. [44]. This was further demonstrated by Altermatt et al. [45]. Therefore, the buried PN junction simultaneously caused higher Auger recombination and surface recombination velocity. Based on the aforementioned experi-

ments, the factors influencing the passivation quality of p^+ poly-Si can be determined: crystallinity, p^+ poly-Si doping concentration (field effect), and indiffusion [10, 11]. However, to use p^+ poly-Si on the front side as a passivated emitter, the thickness of the poly-Si must be reduced to below 50 nm, considering the optical property of parasitic absorption, while shielding sputter damage from indium tin oxide (ITO) deposition [46]. Experiments were further performed to investigate the passivation quality of the thinner 50 nm p^+ poly-Si.

3.2.2. 50 nm poly-Si

The series of experiments and analyses used for 300 nm p^+ poly-Si were repeated for 50 nm p^+ polySi. A pre-test with double-side p^+ poly-Si passivating contacts was conducted before fabricating the cell structures to determine the main factors that control the passivation quality in thin 50 nm poly-Si. The variations were the same as 300 nm poly-Si: annealing temperature and source concentration. As seen in Fig. 3 (b), the passivation quality was lower than 300 nm p^+ poly-Si. However, this tendency was similar to the 300 nm p^+ poly-Si. The highest passivation quality was obtained after annealing at 950 °C for 10 min. The same XRD and SIMS analysis methods were used to investigate the decrease in passivation in the thinner poly-Si layer.

(i) Crystallization of poly-Si

To determine the reasons for the passivation drop with thinner poly-Si, XRD analysis was first performed to compare the grain size. The XRD of 50 nm p^+ poly-Si doped by SOD sources with concentrations of 2% and 4% is shown in Fig. 5 (c). Overall, the intensity dropped and the full width at half maximum (FWHM) was increased compared with that of 300 nm p^+ poly-Si (Fig. 5 (a)), meaning less crystallization. The FWHM values extracted from XRD data are shown in Table A.3. This was because too many boron clusters interfered with crystallization, detailed in the doping concentration profile [47]. Moreover, grain size and iV_{OC} were not correlated. The grain sizes were 1.91 and 7.64 nm for sources with concentrations of 4% and 2%, respectively, while the iV_{OC} was 622.4 mV and 646.7 mV, respectively (Fig. 5 (d)). In summary, the effect of crystallization becomes insignificant in the case that the sample contains poor crystallinity and a buried junction first, although it partially agrees with the 300 nm p^+ poly-Si. In other words, for poly-Si formed with SOD, doping concentration has a more significant effect on passivation quality than crystallinity. The doping profile concentration

was investigated, and it supported the aforementioned assumption.

(ii) Boron doping profile

The 50 nm p^+ poly-Si doping boron profile is shown in Fig. 6 (c). For the 4% source concentration, a BRL was formed inside the poly-Si layer, and no difference in concentration between the poly-Si and bulk was observed. Thus, no field effect occurs. This also indicates a decreased passivation quality [41, 42]. The profile is also similar to the doping of c-Si with no poly-Si layer or tunnel oxide in-between, as shown in Fig. A.11 (a). In addition, this thick BRL is expected to decrease the passivation quality compared with the 300 nm p^+ poly-Si [31]. Conversely, the surface concentration was low for 2%, and boron segregation into the tunnel oxide was observed. Auger recombination, shown in Fig. 6 (d), was also calculated based on the doping profile in Fig. 6 (c). For both source concentrations, indiffusion increased with increasing annealing temperature. Auger recombination increased with increasing annealing temperature and source concentration because of the higher indiffusion into bulk silicon. In addition, comparing the two thicknesses of poly-Si shown in Fig. 6 (b) and (d), the Auger recombination value is larger for 50 nm poly-Si than that for 300 nm poly-Si. Based on the analysis, the drop in passivation for the 50 nm poly-Si compared with the 300 nm poly-Si resulted from the reduced field effect and increased Auger recombination caused by BRL and high indiffusion, respectively.

3.2.3. Pre-test conclusion

In summary, for the 300 nm poly-Si, the passivation quality is either influenced by the grain size, field effect, or indiffusion. An assessment of the particular factor was impossible. The effects change with the annealing conditions and the passivation quality changes with the combination of all the factors. This suggests that all the process parameters are required to achieve high-quality passivation under low interdiffusion conditions. However, outstanding factors are clearly shown for the thinner poly-Si (50 nm). The effect of crystallization of the poly-Si layer on the passivation quality is less significant because high interdiffusion leads to poor passivation quality. Thus, for thin poly-Si, the determining factor was doping profile. Controlling the doping concentration inside the poly-Si for field effect and less indiffusion (reduced Auger recombination) is the key factor in optimizing the thin p^+ poly-Si to be used on the front side of the silicon solar cell as a passivated emitter.

3.3. Both-side poly-Si contact cell results

3.3.1. Simulation results

To optimize the boron doping profile, cell characteristics with different interdiffusion amounts were simulated using QUOKKA to set the standard profile [48, 49]. The doping concentration in poly-Si must be high for high field-effect passivation; however, it cannot exceed the solubility limit [42, 43, 38, 39]. In addition, the depth of the indiffused region must be reduced. In this simulation, the indiffusion depth was changed to determine the maximum indiffusion length, which did not degrade the cell performance, as shown in Fig. A.11 (b). From the simulated LIV results of up to 200 nm, the decrease in efficiency was insignificant; however, the cell efficiency started decreasing when the indiffusion depth exceeded 200 nm. Thus, a constant doping concentration in poly-Si and an indiffusion depth lower than 200 nm are the best conditions for the front-side doping profile of p^+ poly-Si.

3.3.2. Optimization

Experimental groups were split into three directions: further optimization of the annealing time, etch-back of poly-Si, and the insertion of an additional diffusion barrier layer to optimize the doping profile based on simulated results.

(i) Annealing time

From Fig. 6 (c), the diffusion rate of the boron source was extracted, and the optimal annealing time was calculated based on the diffusion rate [39]. The calculated annealing conditions were reduced to 1000 °C for 1 min using a 2% source for a 50 nm poly-Si doping to have a 150 nm boron diffusion into the bulk. As a result, the iV_{OC} result when a 2% source was annealed at 1000 °C for 1 min is shown in Fig. 5 (d). iV_{OC} was increased to 656 mV because of this optimization. The value exceeded any iV_{OC} value obtained with a 50 nm poly-Si, although still lower than that of a 300 nm poly-Si, where the best value was 661.5 mV. The doping profile was also measured to determine the amount of indiffusion and doping concentration, as shown in Fig. 6 (c). The depth of the indiffused region exceeded the calculated value. In addition, owing to the short-time and high-temperature annealing, the diffusion rate of boron supplied by the source at the surface was much higher than that inside the samples, leading to the formation of a BRL inside the poly-Si layer [31] (Fig. 6 (c)). This led to the low iV_{OC} despite the low indiffusion. Therefore, this condition is inappropriate for application.

(ii) Etch back

Because of the poor passivation results with the 50 nm poly-Si, we applied the etch-back method to obtain high-quality passivation with thin poly-Si. Consequently, the iV_{OC} values of the p^+ poly-Si contacts were maintained during the etching of poly-Si and started to decrease (Fig. 7 (a)). This tendency of iV_{OC} as a function of etching time was similar to the etch-back of n^+ poly-Si shown in our previous experiments [10, 11]. Thus, iV_{OC} is expected to start decreasing when the entire poly-Si is etched off, and the tunnel oxide under poly-Si starts etching, leading to poor passivation quality. After confirming the iV_{OC} values, the thickness of the poly-Si before and after etching was validated from the cross-sectional TEM images (Fig. 7 (b)). The poly-Si was effectively etched using the etch-back method; meanwhile, the roughness of the poly-Si surface increased after etching. Owing to this unexpected texture formation on the surface and the non-uniform thickness of the poly-Si layer, additional optimization was conducted to achieve high-quality p^+ poly-Si passivating contacts.

(iii) SiO_x diffusion barrier

Using the phenomenon that boron atoms segregate towards SiO_x [50], a SiO_x diffusion barrier was inserted between the SOD source and poly-Si to control the doping amount. The experimental parameters were determined by calculating the diffusion rate of boron in SiO_x [51] and Fig. 6 (c) [39]. After the deposition of the intrinsic poly-Si, a SiO_x diffusion barrier layer was deposited on top of the intrinsic poly-Si. The SOD source was then applied on top of the doping barrier and annealed in a tube furnace. The experimental values were a doping barrier thickness of 100 nm, a source concentration of 4%, and an annealing time and temperature of 20 min and 950 °C, respectively. As shown in Fig. 8 (b), the passivation quality of the pre-test increased. iV_{OC} was approximately 669 mV, which was higher than any other passivation quality previously achieved with p^+ poly-Si formed with SOD in our study. The doping profiles are shown in Fig. 8 (a) with a comparison of the samples without a doping barrier. It showed a value close to the solubility limit at 950 °C [38, 39]. The indiffusion depth was controlled to approximately 200 nm, which also resulted in reduced Auger recombination. In addition, the field effect is promising because of the significant difference in the doping concentrations in poly-Si and bulk c-Si [33, 42]. The effect of the controlled indiffused depth using a diffusion barrier is shown in Fig. 8 (b) with the improved passivation quality. Based on the pre-test results, silicon solar cells using a thin p^+ poly-Si as an emitter on the front side and n^+ poly-Si on the rear side were fabricated to evaluate the cell performance,

aiming to achieve improved passivation and reduced recombination.

3.3.3. Cell results

Finally, solar cells with both-side poly-Si passivating contacts were manufactured by applying the optimized p^+ poly-Si layer as the front emitter. The cell characteristics of the cells fabricated in this study are listed in Table 1, and a comparison of the cell characteristics of the cells fabricated in this study and those in other studies. Two different anti-reflective coating (ARC) layers were applied to the cell, as shown in Fig. 1 (b) and (c), a both-side poly-Si contact cell with and without ITO, respectively. ITO is widely used for ARC in passivating contacts because of the high contact resistance between the metal and poly-Si. However, in our case, the same metal and passivation structure as a single-side poly-Si contact cell [8] was also fabricated for an exact comparison of the improved passivation quality. As shown in Fig. 9 (a) and Table 1, the cell with a 300 nm p^+ poly-Si used at the front-side showed an efficiency of 15.8%. Owing to the thickness of poly-Si and its parasitic absorption loss, J_{SC} was under 30 mA/cm^2 [52]. A cell with an optimized 50 nm p^+ poly-Si was also fabricated. Here, the efficiency was increased to 17.5%, which is the highest reported for both-side poly-Si contact cells using boron SOD-doped p^+ poly-Si contact on saw-damage-removed flat surfaces (Table 2). The contact resistance of 300 and 50 nm p^+ poly-Si were 19.1 and 8.88 mΩ·cm^2, respectively, before FGA, which comprises of annealing at 600 °C for 30 min in a 10 % H_2/90 % N_2 gas mixture. The contact resistances were reduced to 11.3 and 0.09 mΩ·cm^2 after FGA, respectively (Fig. A.12). This low specific resistance corresponds to a high fill factor of close to 80% in cells with a 300 nm p^+ poly-Si and Al_2O_3/SiN_x. However, the fill factor was lower for the cell with 50 nm p^+ poly-Si, although the contact resistance of the 300 nm poly-Si was higher than that of the 50 nm. This created a discordance. The possible reason for the discordance can be the un-patternend poly-Si layer, as the contact resistance was evaluated by using patterned metal layers on a full-area deposited poly-Si. The high efficiency resulted from the higher V_{OC} achieved, and the higher J_{SC} from the thinner poly-Si and reduced parasitic absorption. This result is promising because both surfaces of the cells were saw-damage-etched with no texturing. Thus, higher efficiency with higher J_{SC} can be expected if textured surfaces are applied to both sides to lower the optical loss. However, this study obtained lower iV_{OC} values compared with Ding et al. [16]. This study differs from theirs in that we used wet chemical oxidation to form a tunnel oxide layer, whereas

they used thermal oxidation. This might have resulted in the lower iV_{OC}, as the iV_{OC} is influenced by the quality of the tunnel oxide [16, 32]. In the future, experiments on the textured surface will be required. Improvements and optimizations on metal contacts using the FGA process and application of selective emitter are suggested to achieve higher cell efficiency. The major problem in developing high-quality textured p^+ poly-Si contacts is achieving a conformal coating of SOD sources on micro-size random pyramid textures. This challenge can be overcome by controlling the texture size or shape, which can be achieved using various technologies, such as nano-texturing, rounding, or inverted pyramid texturing. Furthermore, more detailed analyses of field effects using Hall measurements and pinhole density are necessary, as the dependence of passivation performance on pinhole density was demonstrated by Wietler et al. [53].

Table 1: Cell results of both-side poly-Si contact cells with different poly-Si thicknesses and ARC layers at the front side with a comparison of rear poly-Si contact cell with BBr_3-diffused front emitter

Cell structure	**Thickness of p^+ poly-Si [nm]**	**Dep. power and thickness of ITO**	**iV_{OC} [mV]**	**R_{sh} [Ω/sq]**	**V_{OC} [mV]**	**J_{SC} [mA/cm2]**	**FF [%]**	**PCE [%]**
Both-side poly-Si	300	HP (0.86W/cm^2), 160nm	691	115	657	15.6	33.5	3.44
	300	LP (0.09, 3W/cm^2), 80nm	685	121	656	25.0	67.2	11.0
	300	N/A (Al_2O_3/SiN_x)	685	121	674	29.3	79.9	15.8
	50	N/A (Al_2O_3/SiN_x)	695	119	686	33.3	76.7	17.5
BBr_3 emitter with rear n^+poly-Si	N/A	N/A (Al_2O_3/SiN_x)	683	110	660	34.0	75.8	17.0

Table 2: Summary of research results on boron-doped p^+ poly-Si passivating contacts

Boron-doped p^+ poly-Si					**Characteristics**							**Ref.**
Method	**B conc.** [cm^{-3}]	**R_{sh}** [**Ω/sq**]	**Thickness** [**nm**]	**Anneal temp./time** [**°C/min**]	**iV_{OC}** [**mV**]	**Eff.** [%]	**V_{OC}** [**mV**]	**J_{SC}** [**mA/cm^2**]	**FF** [%]	**ARC**	**Structure** (Passivating Contact)	
B ink	1E19-1E20	284	50	950/10	700	-	-	-	-	-	-	[18]
BBr_3	1E20	30-1000	30-90	870-980/30	-	-	-	-	-	-	-	[19]
BBr_3	3E20	20-100	100	-	685	20.6	677	38.5	79.0	SiN_x	Both sides	[20]
BBr_3	-	-	250	850-950/-	713	-	-	-	-	-	-	[21]
Implantation	3E20	-	45	900-1050/10+10 sec	705	-	-	-	-	-	-	[22]
Implantation	2E19	1000	15	850/10	696	19.2	709	33.4	83	AZO/ITO	Both sides	[54]
Implantation	5E15	-	145	900/30	-	-	-	-	-	-	-	[23]
Implantation	1E20	-	250	-/5-30	716	22.1	709	40.7	76.6	SiN_x	IBC	[24]
Implantation	-	-	160	900/30	-	26.1	726	42.6	84.2	AlO_x/SiN_x/SiO_x	IBC	[25]
In-situ (LPCVD)	7E19-4E20	¡400	-	800-1000/30	-	-	-	-	-	-	-	[26]
In-situ (PECVD)	-	-	30	200-950/30	-	-	-	-	-	-	-	[27]
In-situ (PECVD)	1E21	-	25	800/30	736	-	-	-	-	-	-	[28]
B SOD	1E20	50-300	100-230	850-1000/10-90	720	-	-	-	-	-	-	[16]
B SOD	2E20	90-121	50-300	850-1000/10-30	670	17.5	686	33.3	76.7	SiN_x/AlO_x	Both sides	This work

4. Summary

The passivation quality of p^+ poly-Si/SiO $_x$/c-Si passivating contacts using boron SOD was investigated. This study used the p^+ poly-Si contact on the front side as a passivated emitter to reduce the emitter recombination formed by the conventional BBr_3-diffused emitter. Based on the the pre-test results with thick p^+ poly-Si layers, the passivation quality of p^+ poly-Si and tunnel oxide are influenced by the crystallization of poly-Si (grain size), indiffusion of boron atoms into the bulk silicon, and doping concentration in the poly-Si layer (field effect). Experiments were further conducted with thinner poly-Si. The dominant factors among the three were the indiffusion and doping concentration in poly-Si. By adding a diffusion barrier, the doping process was further optimized by controlling the amount of boron diffused from the SOD source. This led to a high iV_{OC} of up to 670 mV. Both-side poly-Si contact solar cells with p^+ and n^+ poly-Si passivating contacts on the front and rear sides were fabricated, respectively. The both-side poly-Si cell showed a higher V_{OC} through a lower recombination loss from the emitter compared with a reference cell with a BBr_3-diffused emitter and rear n^+ poly-Si contact. Both-side poly-Si cell efficiencies of 15.8% and 17.5% were achieved with 300 nm and 50 nm p^+ poly-Si, respectively. Furthermore, the improvement in passivation quality using SOD p^+ poly-Si compared with the BBr_3-diffused p^+emitter showed a high possibility of reaching an even higher passivation quality if the doping process is more specifically optimized. In addition, this cell structure is a high potential candidate for tandem applications, as it shows reduced emitter recombination. Textured surfaces, FGA for improved metal contacts, and selective-emitter technology can be applied in the future, which will increase the cell efficiency.

5. Acknowledgment

This study was supported by the """Human Resources Program in Energy Technology" ""of the Korea Institute of Energy Technology Evaluation and Planning (KETEP). Financial resources were received from the Ministry of Trade, Industry & Energy, Republic of Korea. (No. 20204010600470). Furthermore, the New & Renewable Energy Core Technology Program of the Korea Institute of Energy Technology Evaluation and Planning (KETEP) was granted financial support from the Ministry of Trade, Industry & Energy, Republic of Korea. (No. 20203030010300)

6. Conflict of interest

The authors declare that they have no conflicts of interest.

Appendix A. Supplementary

Table A.3: Full width at half maximum (FWHM) and extracted grain size (GS) values of p^+ poly-Si passivating contacts

poly-Si thickness (nm)	SOD concentration	Annealing condition	(111)		(220)		(311)		(422)		Average of GS (nm)
			FWHM	GS (nm)	FWHM	GS (nm)	FWHM	GS (nm)	FWHM	GS (nm)	
300	4%	950 °C 10 min	1.553	10.55	0.397	43.73	0.700	25.75	0.928	23.87	25.97
	4%	950 °C 20 min	1.871	8.75	0.531	32.68	1.153	15.61	1.068	20.70	19.44
	4%	950 °C 30 min	0.167	98.10	0.480	36.14	0.819	21.98	0.443	49.97	51.54
50	4%	950 °C 10 min	12.207	1.34	7.002	2.48	-	-	-	-	1.91
	2%	950 °C 10 min	1.475	11.10	-	-	4.287 -	4.18	-	-	7.64
	2%	1000 °C 10 min	2.115	7.74	0.683	25.41	1.152	15.64	-	-	16.27

References

[1] K. Yoshikawa, H. Kawasaki, W. Yoshida, T. Irie, K. Konishi, K. Nakano, T. Uto, D. Adachi, M. Kanematsu, H. Uzu, et al., Silicon heterojunction solar cell with interdigitated back contacts for a photoconversion efficiency over 26%, Nature energy 2 (5) (2017) 1–8.

[2] S. De Wolf, A. Descoeudres, Z. C. Holman, C. Ballif, High-efficiency silicon heterojunction solar cells: A review, green 2 (1) (2012) 7–24.

[3] J. Melskens, B. W. van de Loo, B. Macco, M. F. Vos, J. Palmans, S. Smit, W. Kessels, Concepts and prospects of passivating contacts for crystalline silicon solar cells, in: 2015 IEEE 42nd Photovoltaic Specialist Conference (PVSC), IEEE, 2015, pp. 1–6.

[4] F. Feldmann, M. Simon, M. Bivour, C. Reichel, M. Hermle, S. Glunz, Carrier-selective contacts for si solar cells, Applied Physics Letters 104 (18) (2014) 181105.

[5] C. Reichel, F. Feldmann, R. Müller, R. C. Reedy, B. G. Lee, D. L. Young, P. Stradins, M. Hermle, S. W. Glunz, Tunnel oxide passivated contacts formed by ion implantation for applications in silicon solar cells, Journal of Applied Physics 118 (20) (2015) 205701.

[6] C. Lee, S. Bae, H. Park, D. Choi, H. Song, H. Lee, Y. Ohshita, D. Kim, Y. Kang, H.-S. Lee, Properties of thermally evaporated titanium dioxide as an electron-selective contact for silicon solar cells, Energies 13 (3) (2020) 678.

[7] U. Würfel, A. Cuevas, P. Würfel, Charge carrier separation in solar cells, IEEE Journal of Photovoltaics 5 (1) (2014) 461–469.

[8] A. Richter, R. Müller, J. Benick, F. Feldmann, B. Steinhauser, C. Reichel, A. Fell, M. Bivour, M. Hermle, S. W. Glunz, Design rules for high-efficiency both-sides-contacted silicon solar cells with balanced charge carrier transport and recombination losses, Nature Energy 6 (4) (2021) 429–438.

[9] C. Hollemann, F. Haase, M. Rienäcker, V. Barnscheidt, J. Krügener, N. Folchert, R. Brendel, S. Richter, S. Großer, E. Sauter, et al., Separating the two polarities of the polo contacts of an 26.1%-efficient ibc solar cell, Scientific reports 10 (1) (2020) 1–15.

[10] H. Park, S. Bae, S. J. Park, J. Y. Hyun, C. H. Lee, D. Choi, D. Kang, H. Han, Y. Kang, H.-S. Lee, et al., Role of polysilicon in poly-si/sio x passivating contacts for high-efficiency silicon solar cells, RSC advances 9 (40) (2019) 23261–23266.

[11] H. Park, H. Park, S. J. Park, S. Bae, H. Kim, J. W. Yang, J. Y. Hyun, C. H. Lee, S. H. Shin, Y. Kang, et al., Passivation quality control in poly-si/siox/c-si passivated contact solar cells with 734 mv implied open circuit voltage, Solar Energy Materials and Solar Cells 189 (2019) 21–26.

[12] H. Park, Y. Lee, S. J. Park, S. Bae, S. Kim, D. Oh, J. Park, Y. Kim, H. Guim, Y. Kang, et al., Tunnel oxide passivating electron contacts for high-efficiency n-type silicon solar cells with amorphous silicon passivating hole contacts, Progress in Photovoltaics: Research and Applications 27 (12) (2019) 1104–1114.

[13] H. Hieslmair, L. Mandrell, I. Latchford, M. Chun, J. Sullivan, B. Adibi, High throughput ion-implantation for silicon solar cells, Energy Procedia 27 (2012) 122–128.

[14] A. Dastgheib-Shirazi, M. Steyer, G. Micard, H. Wagner, P. P. Altermatt, G. Hahn, Relationships between diffusion parameters and phosphorus

precipitation during the pocl3 diffusion process, Energy Procedia 38 (2013) 254–262.

[15] R. Chen, H. Wagner, A. Dastgheib-Shirazi, M. Kessler, Z. Zhu, V. Shutthanandan, P. P. Altermatt, S. T. Dunham, A model for phosphosilicate glass deposition via pocl3 for control of phosphorus dose in si, Journal of Applied Physics 112 (12) (2012) 124912.

[16] Z. Ding, T. N. Truong, H. T. Nguyen, D. Yan, X. Zhang, J. Yang, Z. Wang, P. Zheng, Y. Wan, D. Macdonald, J. Stuckelberger, Boron spin-on doping for poly-si/siox passivating contacts, ACS Applied Energy Materials 4 (5) (2021) 4993–4999. doi:10.1021/acsaem.1c00550.

[17] J. Y. Lee, S. H. Lee, Boron back surface field using spin-on dopants by rapid thermal processing, JOURNAL-KOREAN PHYSICAL SOCIETY 44 (2004) 1581–1586.

[18] Z. Kiaee, C. Reichel, F. Feldmann, M. Jahn, J. Huyeng, R. Keding, M. Hermle, F. Clement, et al., Printed dopant sources for locally-doped siox/poly-si passivating contacts, in: Proc. Eur. Photovolt. Specialist Conf., 2018, pp. 1–6.

[19] D. Yan, A. Cuevas, Y. Wan, J. Bullock, Passivating contacts for silicon solar cells based on boron-diffused recrystallized amorphous silicon and thin dielectric interlayers, Solar Energy Materials and Solar Cells 152 (2016) 73–79.

[20] R. Naber, M. Lenes, J. Luchies, J. Zhai, D. Liu, Z. Wang, F. Li, Bbr3 emitter passivation by ultra-thin boron doped lpcvd polysilicon layers, in: Proceedings of the 33rd European Photovoltaic Solar Energy and Conference,(Amsterdam, the Netherlands, 2017), 2017, pp. 472–475.

[21] Z. P. Ling, Z. Xin, P. Wang, R. Sridharan, C. Ke, R. Stangl, Double-sided passivated contacts for solar cell applications: An industrially viable approach toward 24% efficient large area silicon solar cells, in: Silicon Materials, IntechOpen, 2019, p. 89.

[22] F. Feldmann, J. Schoen, J. Niess, W. Lerch, M. Hermle, Studying dopant diffusion from poly-si passivating contacts, Solar Energy Materials and Solar Cells 200 (2019) 109978.

[23] S. Reiter, N. Koper, R. Reineke-Koch, Y. Larionova, M. Turcu, J. Krügener, D. Tetzlaff, T. Wietler, U. Höhne, J.-D. Kähler, et al., Parasitic absorption in polycrystalline si-layers for carrier-selective front junctions, Energy Procedia 92 (2016) 199–204.

[24] G. Yang, Y. Zhang, P. Procel, A. Weeber, O. Isabella, M. Zeman, Poly-si (o) x passivating contacts for high-efficiency c-si ibc solar cells, Energy Procedia 124 (2017) 392–399.

[25] F. Haase, C. Hollemann, S. Schäfer, A. Merkle, M. Rienäcker, J. Krügener, R. Brendel, R. Peibst, Laser contact openings for local poly-si-metal contacts enabling 26.1%-efficient polo-ibc solar cells, Solar Energy Materials and Solar Cells 186 (2018) 184–193.

[26] J. Krügener, D. Tetzlaff, Y. Barnscheidt, Y. Larionova, S. Reiter, M. Turcu, T. Wietler, R. Peibst, U. Höhne, J.-D. Kähler, Electrical deactivation of boron in p+-polycrystalline silicon/siox/crystalline silicon passivating contacts for silicon solar cells, in: 2016 21st International Conference on Ion Implantation Technology (IIT), IEEE, 2016, pp. 1–4.

[27] W. Liu, X. Yang, J. Kang, S. Li, L. Xu, S. Zhang, H. Xu, J. Peng, F. Xie, J.-H. Fu, et al., Polysilicon passivating contacts for silicon solar cells: interface passivation and carrier transport mechanism, ACS Applied Energy Materials 2 (7) (2019) 4609–4617.

[28] M. Hayes, B. Martel, G. W. Alam, H. Lignier, S. Dubois, E. Pihan, O. Palais, Impurity gettering by boron-and phosphorus-doped polysilicon passivating contacts for high-efficiency multicrystalline silicon solar cells, physica status solidi (a) 216 (17) (2019) 1900321.

[29] P. Rothhardt, C. Demberger, A. Wolf, D. Biro, Co-diffusion from apcvd bsg and pocl3 for industrial n-type solar cells, Energy Procedia 38 (2013) 305–311.

[30] T. Chan, C. Mai, Diffusion of boron, phosphorus, arsenic, and antimony into, Proceedings of the IEEE 58 (4) (1970) 588–589.

[31] B. Singha, C. S. Solanki, Impact of a boron rich layer on minority carrier lifetime degradation in boron spin-on dopant diffused n-type crystalline silicon solar cells, Semiconductor Science and Technology 31 (3) (2016) 035009.

[32] H. Kim, S. Bae, K.-s. Ji, S. M. Kim, J. W. Yang, C. H. Lee, K. D. Lee, S. Kim, Y. Kang, H.-S. Lee, et al., Passivation properties of tunnel oxide layer in passivated contact silicon solar cells, Applied Surface Science 409 (2017) 140–148.

[33] K. R. McIntosh, P. P. Altermatt, A freeware 1d emitter model for silicon solar cells, in: 2010 35th IEEE Photovoltaic Specialists Conference, IEEE, 2010, pp. 002188–002193.

[34] M. Miyake, Diffusion of boron into silicon from borosilicate glass using rapid thermal processing, Journal of the Electrochemical Society 138 (10) (1991) 3031.

[35] J. F. Watts, J. Wolstenholme, An introduction to surface analysis by XPS and AES, John Wiley & Sons, 2019.

[36] D. Yan, A. Cuevas, Y. Wan, J. Bullock, Passivating contacts for silicon solar cells based on boron-diffused recrystallized amorphous silicon and thin dielectric interlayers, Solar Energy Materials and Solar Cells 152 (2016) 73–79.

[37] P. Scherrer, Bestimmung der inneren struktur und der größe von kolloidteilchen mittels röntgenstrahlen, in: Kolloidchemie Ein Lehrbuch, Springer, 1912, pp. 387–409.

[38] G. Vick, K. Whittle, Solid solubility and diffusion coefficients of boron in silicon, Journal of the electrochemical society 116 (8) (1969) 1142.

[39] R. C. Jaeger, Introduction to microelectronic fabrication, Addison-Wesley Longman Publishing Co., Inc., 1987.

[40] G. Limodio, G. Yang, Y. De Groot, P. Procel, L. Mazzarella, A. W. Weber, O. Isabella, M. Zeman, Implantation-based passivating contacts for crystalline silicon front/rear contacted solar cells, Progress in Photovoltaics: research and applications 28 (5) (2020) 403–416.

[41] J. Melskens, B. W. van de Loo, B. Macco, L. E. Black, S. Smit, W. Kessels, Passivating contacts for crystalline silicon solar cells: From concepts and materials to prospects, IEEE Journal of Photovoltaics 8 (2) (2018) 373–388.

[42] S. Glunz, D. Biro, S. Rein, W. Warta, Field-effect passivation of the sio 2 si interface, Journal of Applied Physics 86 (1) (1999) 683–691.

[43] J. Stuckelberger, G. Nogay, P. Wyss, A. Ingenito, C. Allebé, J. Horzel, B. A. Kamino, M. Despeisse, F.-J. Haug, P. Löper, et al., Recombination analysis of phosphorus-doped nanostructured silicon oxide passivating electron contacts for silicon solar cells, IEEE Journal of Photovoltaics 8 (2) (2018) 389–396.

[44] P. Wyss, J. Stuckelberger, G. Nogay, J. Horzel, Q. Jeangros, I. Mack, M. Lehmann, X. Niquille, C. Allebé, M. Despeisse, et al., A mixed-phase sio x hole selective junction compatible with high temperatures used in industrial solar cell manufacturing, IEEE Journal of Photovoltaics 10 (5) (2020) 1262–1269.

[45] P. P. Altermatt, J. O. Schumacher, A. Cuevas, M. J. Kerr, S. W. Glunz, R. R. King, G. Heiser, A. Schenk, Numerical modeling of highly doped si: P emitters based on fermi–dirac statistics and self-consistent material parameters, Journal of Applied Physics 92 (6) (2002) 3187–3197.

[46] L. Tutsch, F. Feldmann, J. Polzin, C. Luderer, M. Bivour, A. Moldovan, J. Rentsch, M. Hermle, Implementing transparent conducting oxides by dc sputtering on ultrathin siox/poly-si passivating contacts, Solar Energy Materials and Solar Cells 200 (2019) 109960.

[47] N. Ren, Z. Liu, Q. Wang, Investigating the effects of microstructure on optical properties of different kinds of polysilicon thin films, Physics Letters A 379 (16-17) (2015) 1153–1160.

[48] A. Fell, K. C. Fong, K. R. McIntosh, E. Franklin, A. W. Blakers, 3-d simulation of interdigitated-back-contact silicon solar cells with quokka including perimeter losses, IEEE Journal of Photovoltaics 4 (4) (2014) 1040–1045.

[49] H. Song, C. Lee, J. Hyun, S.-W. Lee, D. Choi, D. Pyun, J. Nam, S.-H. Jeong, J. Kim, S. Bae, et al., Monolithic perovskite-carrier selective contact silicon tandem solar cells using molybdenum oxide as a hole selective layer, Energies 14 (11) (2021) 3108.

[50] J. Colby, L. Katz, Boron segregation at si-sio2 interface as a function of temperature and orientation, Journal of the Electrochemical Society 123 (3) (1976) 409.

[51] S. Horiuchi, J. Yamaguchi, Diffusion of boron in silicon through oxide layer, Japanese Journal of Applied Physics 1 (6) (1962) 314.

[52] S. Reiter, N. Koper, R. Reineke-Koch, Y. Larionova, M. Turcu, J. Krügener, D. Tetzlaff, T. Wietler, U. Höhne, J.-D. Kähler, et al., Parasitic absorption in polycrystalline si-layers for carrier-selective front junctions, Energy Procedia 92 (2016) 199–204.

[53] T. Wietler, D. Tetzlaff, J. Krügener, M. Rienäcker, F. Haase, Y. Larionova, R. Brendel, R. Peibst, Pinhole density and contact resistivity of carrier selective junctions with polycrystalline silicon on oxide, Applied Physics Letters 110 (25) (2017) 253902.

[54] F. Feldmann, C. Reichel, R. Müller, M. Hermle, The application of poly-si/siox contacts as passivated top/rear contacts in si solar cells, Solar Energy Materials and Solar Cells 159 (2017) 265–271.

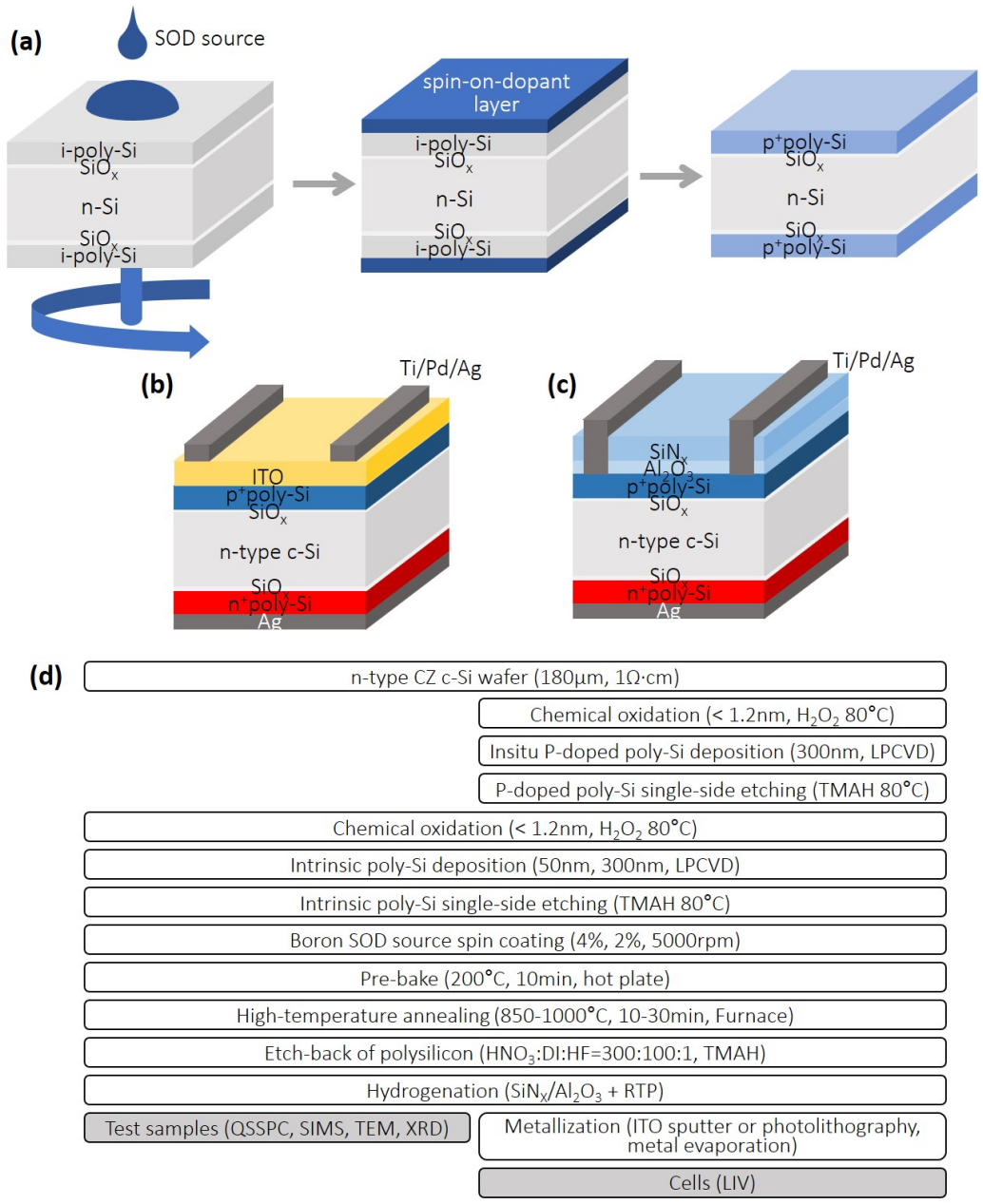

Figure 1: (a) Schematics of test sample structure and experimental process, (b) cell structure with a different ARC of ITO and (c) Al_2O_3/SiN_x, and (d) process flow chart for test samples and solar cells

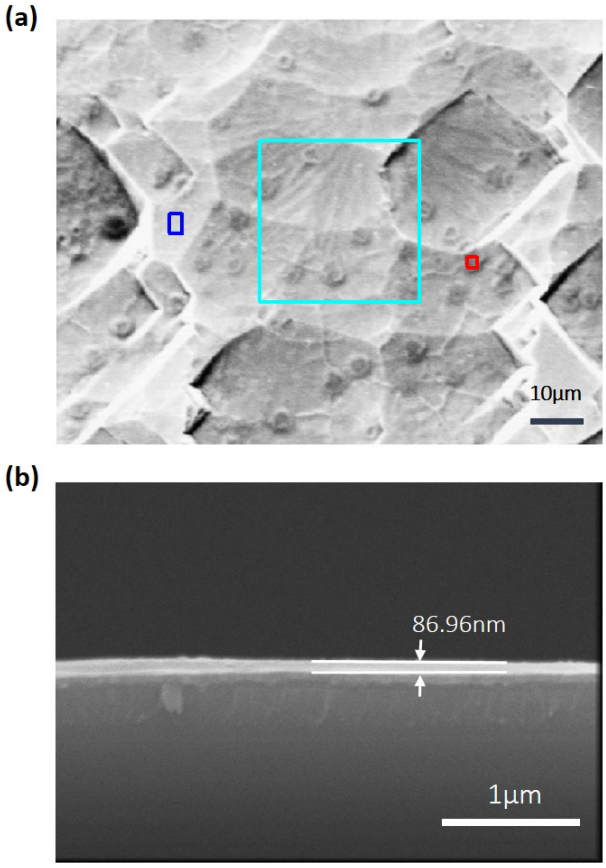

Figure 2: (a) Plan-view and (b) cross-sectional SEM image of the SOD source layer

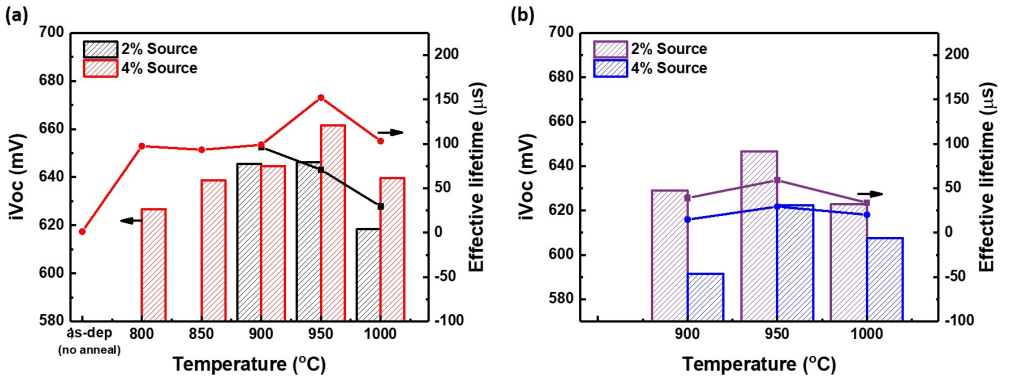

Figure 3: Passivation quality (iV$_{OC}$ and lifetime) of p$^+$ poly-Si contacts with a variation in SOD concentration and annealing temperature at different poly-Si thicknesses. (a) 300 nm and (b) 50 nm poly-Si

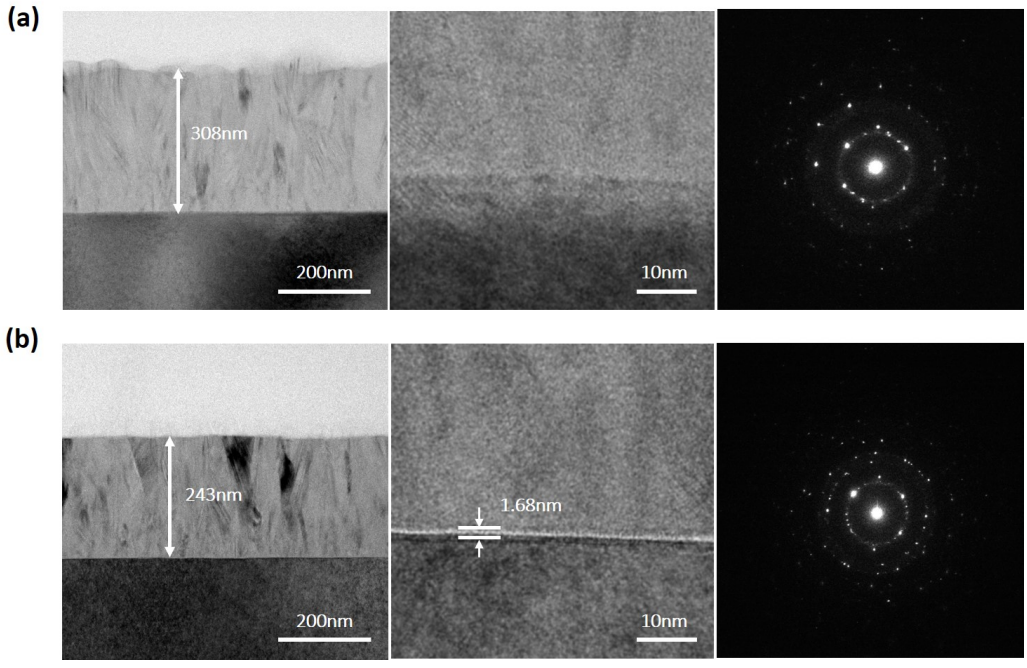

Figure 4: (a) Cross-sectional TEM images and diffraction patterns of intrinsic poly-Si before annealing and (b) p$^+$ poly-Si after annealing at 950 °C for 10 min

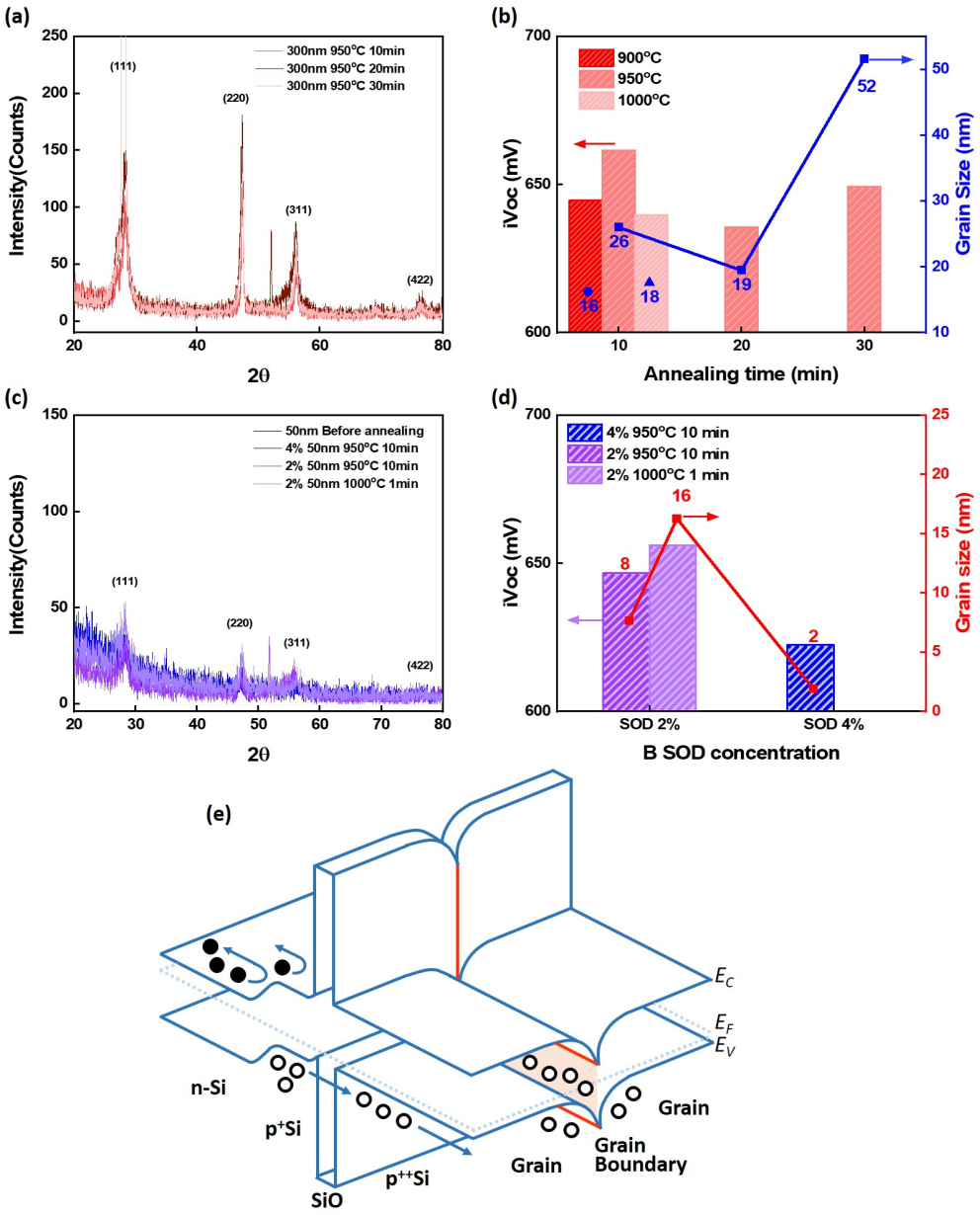

Figure 5: 300 nm p^+ poly-Si: (a) XRD patterns and (b) passivation quality and grain size according to the XRD patterns. 50 nm p^+ poly-Si: (c) XRD patterns and (d) passivation quality and grain size. (e) Schematic energy band diagram of p^+ poly-Si/SiO_x/n-Si with indiffused p^+Si region

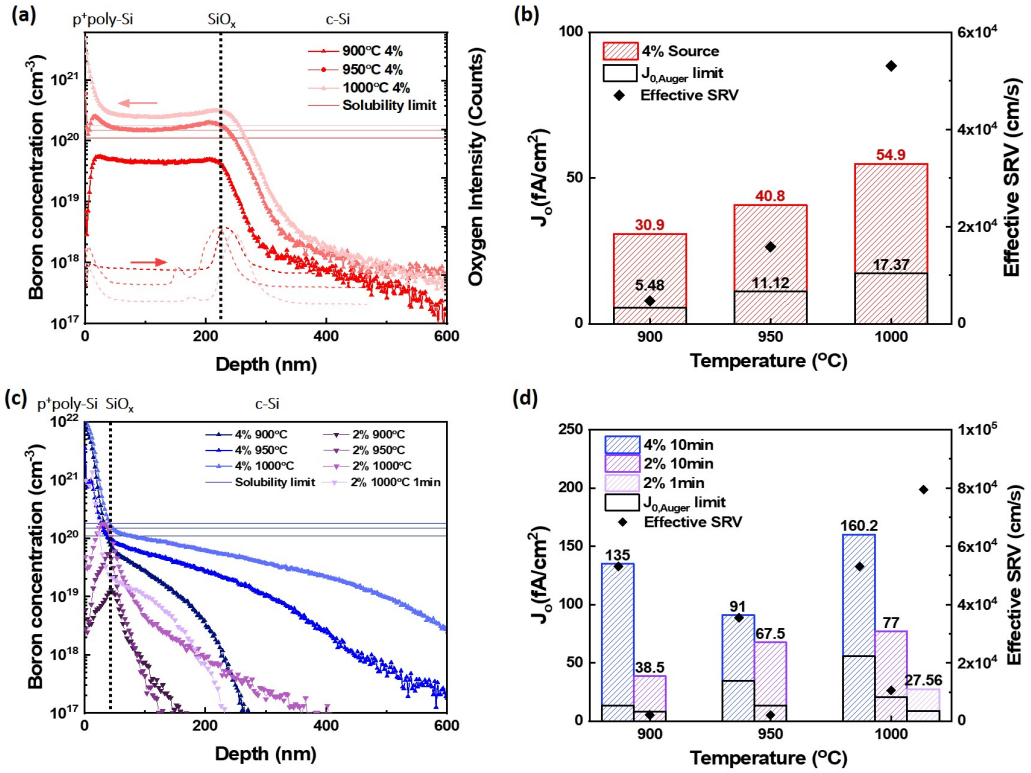

Figure 6: 300 nm p^+ poly-Si: (a) Doping concentration profile with solubility limit, (b) measured J_0, the contribution of Auger recombination (estimated from SIMS profile with EDNA2), and effective SRV at different annealing temperatures, 50 nm p^+ poly-Si: (c) Doping concentration profile with solubility limit, (d) measured J_0, the contribution of Auger recombination, and effective SRV as a function of annealing temperature

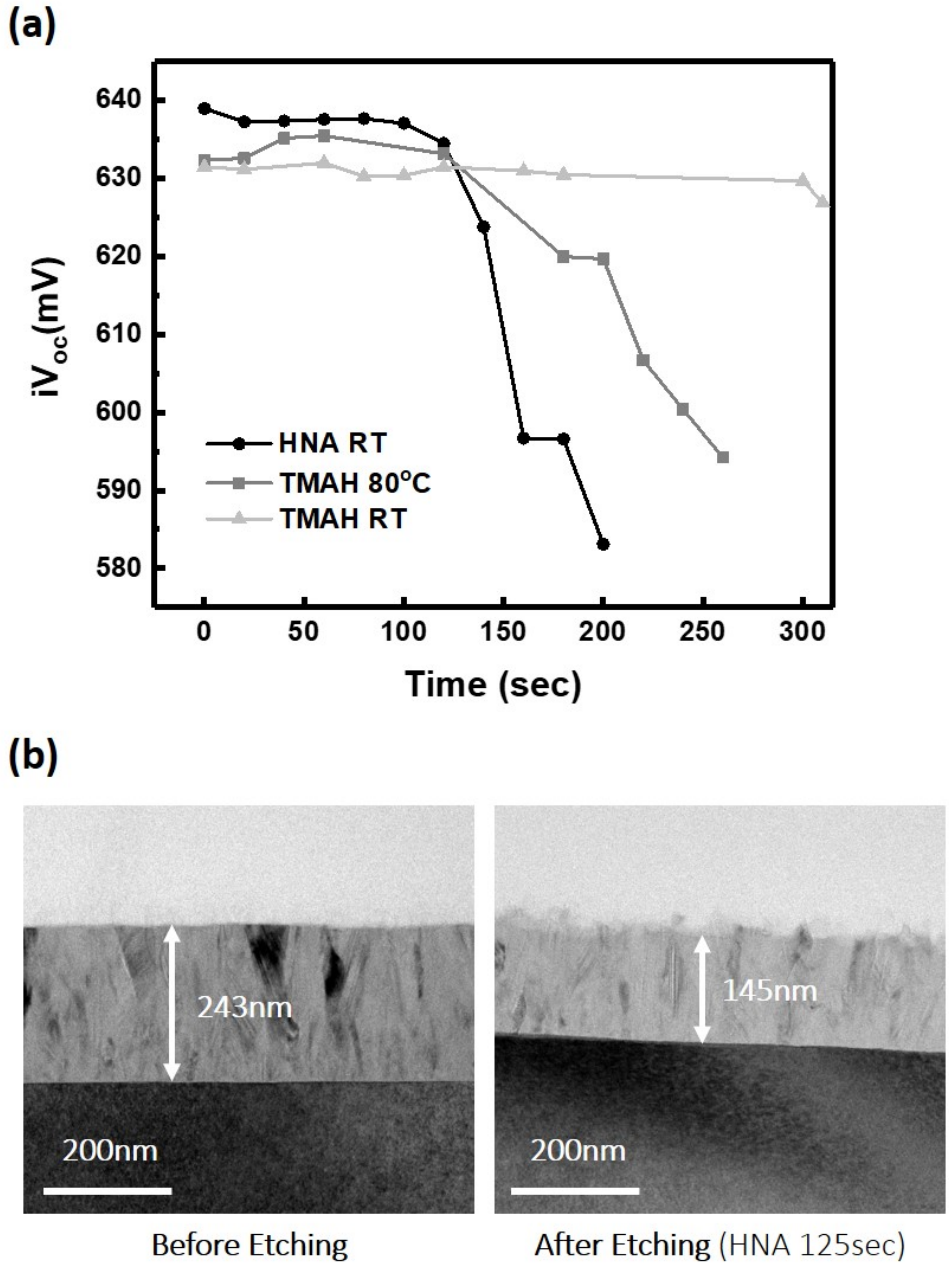

Figure 7: (a) iV_{OC} as a function of etching time with different etch-back solutions, and (b) cross-sectional TEM images of the 300 nm p^+ poly-Si contacts before and after etching

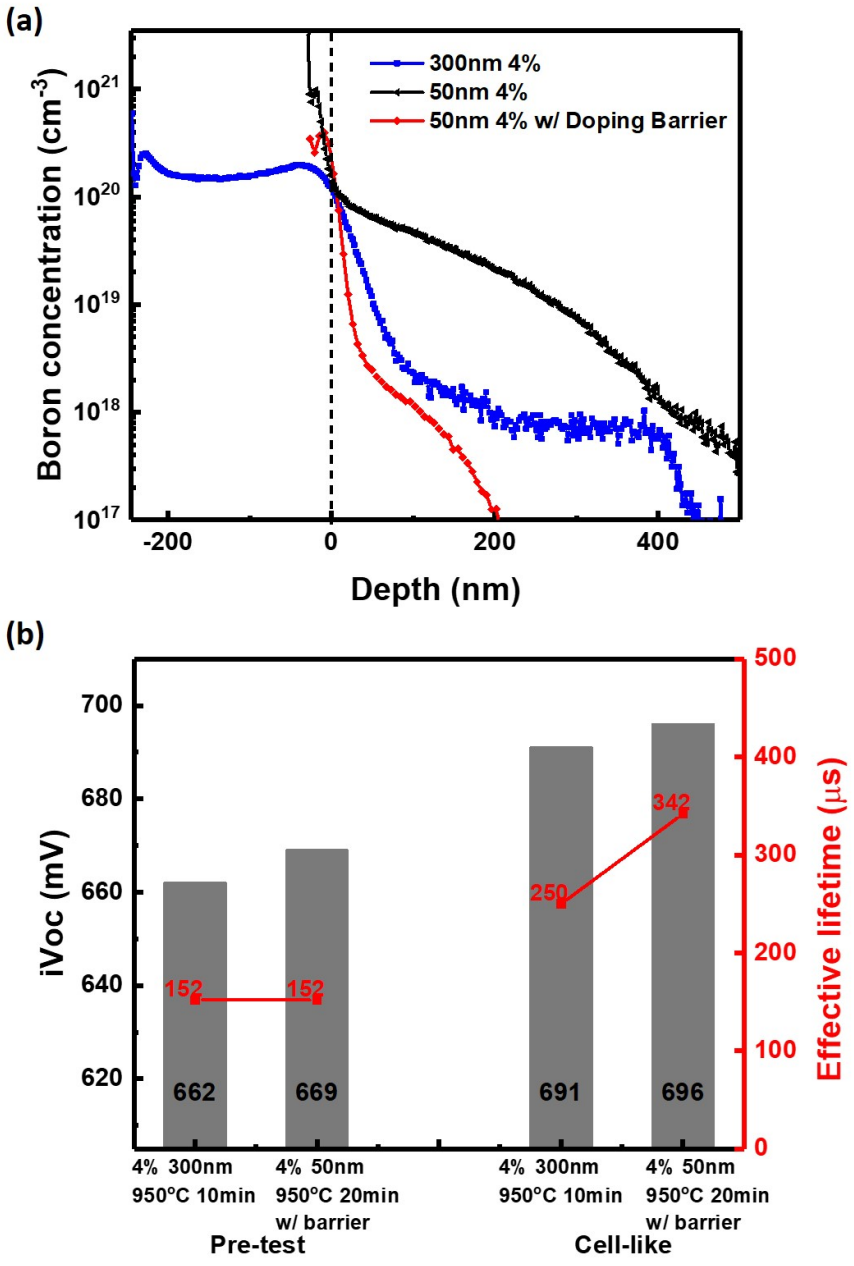

Figure 8: (a) Doping profile and (b) pre-test and cell-like passivation quality results, comparing the cases with and without a diffusion barrier

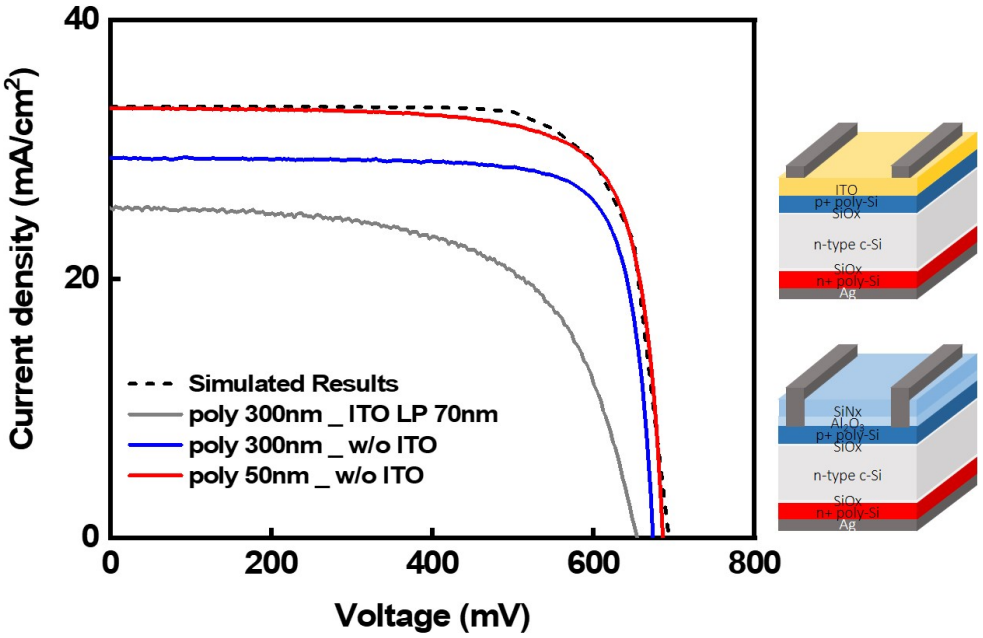

Figure 9: LIV curve of both-side poly-Si contact cell with different p^+ poly-Si thicknesses and ARC layers (ITO and Al_2O_3/SiN_x) at the front side, and corresponding schematic cell structures

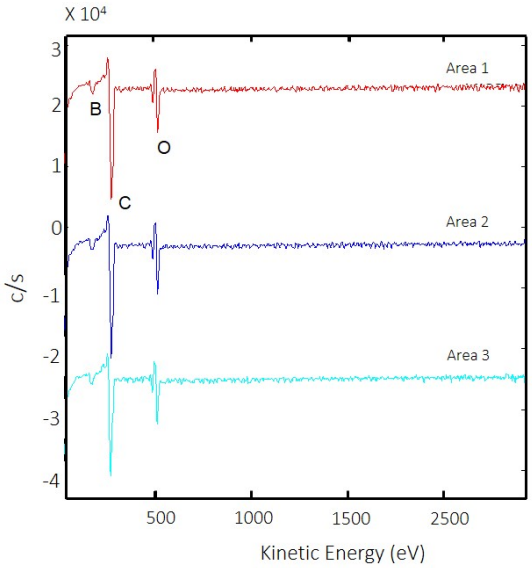

Figure A.10: AES spectrum in three different areas marked in Fig. 2 (a)

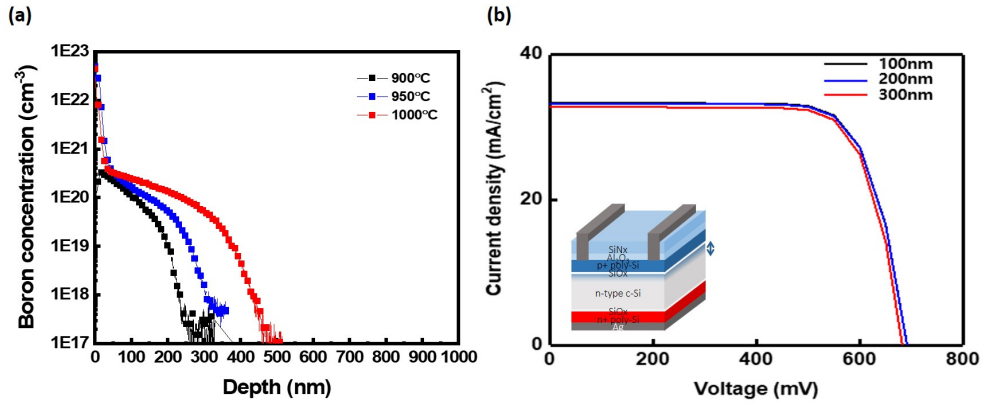

Figure A.11: (a) Boron concentration profile using a 4% SOD on a bare c-Si wafer and (b) Simulated LIV results with a 50 nm p^+ poly-Si at the front side for different indiffusion depths

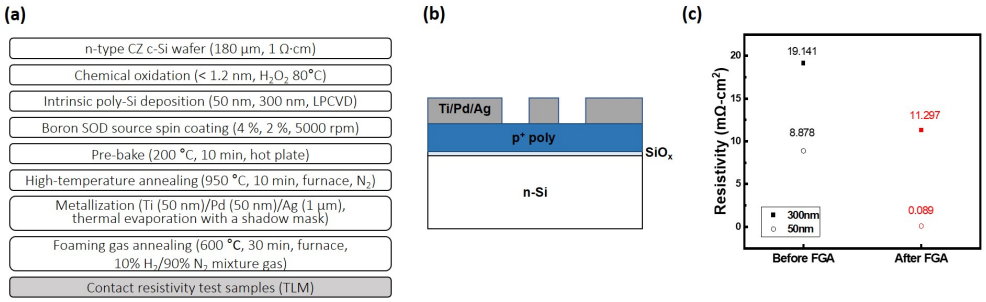

Figure A.12: (a) Process flow chart for the specific contact resistance samples, (b) schematic sample structure with the transfer length method patterned metal electrodes, and (c) contact resistance comparison before and after the FGA process, for 300 and 50 nm p^+ poly-Si